FINAL CALIBRATION OF THE BERKELEY EXTREME AND FAR-ULTRAVIOLET SPECTROMETER ON THE ORFEUS-SPAS I AND II MISSIONS[1]

W. VAN DYKE DIXON[2], JEAN DUPUIS[2], AND MARK HURWITZ

Space Sciences Laboratory
University of California, Berkeley, Berkeley, California 94720-7450
vand@ssl.berkeley.edu, jdupuis@ssl.berkeley.edu, markh@ssl.berkeley.edu
To appear in Publications of the Astronomical Society of the Pacific, *January 2002*

ABSTRACT

The Berkeley Extreme and Far-Ultraviolet Spectrometer (BEFS) flew as part of the ORFEUS telescope on the *ORFEUS-SPAS I* and *II* space-shuttle missions in 1993 and 1996, respectively. The data obtained by this instrument have now entered the public domain. To facilitate their use by the astronomical community, we have re-extracted and re-calibrated both data sets, converted them into a standard (FITS) format, and placed them in the Multimission Archive at Space Telescope (MAST). Our final calibration yields improved wavelength scales and effective-area curves for both data sets.

Subject headings: stars: atmospheres — white dwarfs: individual (G 191–B2B, HZ 43) — ultraviolet: stars — instrumentation: spectrographs — astronomical data bases: miscellaneous

1. INTRODUCTION

The Berkeley Extreme and Far-Ultraviolet Spectrometer (BEFS) flew aboard the ORFEUS telescope on the *ORFEUS-SPAS I* and *II* space-shuttle missions in 1993 September and 1996 November/December, respectively. The instrument returned 109 observations of 75 astrophysical objects on the first mission and 223 observations of 108 astrophysical objects on the second. We have performed a new extraction and calibration of the BEFS spectra from both missions. The resulting data set offers an improved flux calibration and wavelength solution in a standard FITS data format. The extracted spectra, together with the photon-event lists from which they were derived, are available through the archives of the Space Telescope Science Institute. Now in the public domain, these data will contribute to studies of the interstellar medium; early-type, coronal, and white-dwarf stars; cataclysmic variables; active galactic nuclei; and the emission processes of the earth's outer atmosphere. In addition, they will be useful to investigators planning observations with the *Far Ultraviolet Spectroscopic Explorer (FUSE)*.

In this paper, we discuss the final calibration of the Berkeley spectrometer. We describe the format of the resulting data files and the software tools provided for their analysis.

2. DATA EXTRACTION AND CALIBRATION

2.1. *The Instrument*

The BEFS sits at the prime focus of the 1-m ORFEUS telescope (Grewing et al. 1991) To improve the resolution and reduce astigmatism, the spectrometer employs mechanically-ruled diffraction gratings with varied line spacing in a non-Rowland mounting. Four such gratings, together with an optic that feeds a fine-guidance sensor, are arranged in an annulus at the end of the spectrom-

eter opposite the entrance aperture as shown in Fig. 1. Each grating disperses a unique spectral region (Table 1) onto one of two microchannel-plate detectors located near the focal plane of the spectrometer. Together, the four gratings simultaneously span the wavelength region from approximately 380 to 1220 Å at a spectral resolution of $\lambda/\Delta\lambda \sim 4600$ for point sources. A detailed discussion of the instrument's design may be found in Hurwitz & Bowyer (1986, 1996). Its performance on the *ORFEUS-SPAS I* mission is described in Hurwitz & Bowyer (1995) and on the *ORFEUS-SPAS II* mission in Hurwitz et al. (1998).

Spectra A and B are imaged by Detector 0, spectra C and D by Detector 1 (Fig. 2). Between the 1993 and 1996 flights, the four gratings were shifted in their mountings to optimize their wavelength coverage. On the second flight, both spectra A and B span the important He I edge at 504 Å, and spectrum D extends to wavelengths just longer than the Lyman α line at 1216 Å. On the 1993 flight, both detectors were powered for nearly all observations, but on the 1996 flight, Detector 0 was powered only during observations of known EUV sources in order to minimize its contribution (mostly in the form of detector background events) to the telemetry stream. For both missions, Grating A and B spectra were extracted only for selected targets.

An unplanned change in the spectrograph for the 1996 flight was an apparent shift of one or both of Gratings A and B; their spectra intersect, forming an "X" on the detector (Fig. 2). The most likely reason for the grating shift is "creep" in the viton material that was employed to constrain the optics within their holders. Because these two optics were not de-mounted between flights, the viton, which is normally under a small shear load, may have crept or relaxed, leaving the grating susceptible to shifts under the stress of launch. Gratings C and D show no

---

[2] Present address: Department of Physics and Astronomy, The Johns Hopkins University, Baltimore, MD 21218

Table 1
Berkeley Extreme and Far-Ultraviolet Spectrometer Gratings

Grating	Central Groove Density (mm^{-1})	Bandpass (Å)		Coating	
		1993	1996	1993	1996
A	6000.0	380–510	390–520	Evaporated Ir	Evaporated Ir
B	4550.0	514–687	500–670	Evaporated Ir	Evaporated Ir
C	3450.4	658–894	680–910	Evaporated Ir	Sputtered SiC
D	2616.6	865–1175	910–1220	Evaporated Ir	Sputtered SiC

NOTE.—The geometry of each grating/detector system is identical save for rotation about the Z axis and/or reflection through the detector midplane. The incidence angle is $12°$. The wavelength coverage ($\lambda_{MAX}/\lambda_{MIN}$) of each grating is identical, as is the ratio of central wavelength to groove density.

such shift, perhaps because they were de-mounted after the first mission for overcoating with SiC.

On the 1993 flight, a single aperture $20''$ in diameter was used for all astronomical observations. On the 1996 flight, the spectrograph was equipped with a diaphragm selection blade with three scientifically-useful positions: Position 1 contains a single on-axis aperture $20''$ in diameter; it was rarely used for science observations. Position 2 contains a single on-axis aperture $10'$ in diameter, used during the initial star tracker/telescope co-alignment and for some observations of diffuse backgrounds and extended objects. Position 3, with which most science observations were obtained, contains three apertures. Targets were usually placed in the on-axis aperture, which is $26''$ in diameter. A second clear aperture, about 1.4 times larger in area and displaced by $2'.4$, was designed to obtain simultaneous airglow observations, although in crowded fields an astrophysical source was occasionally observed. A third aperture, $120''$ in diameter, was displaced by $5'.0$ and covered by a tin filter approximately 1500 Å thick. The tin filter is virtually opaque to FUV radiation and was employed primarily for observations of the EUV spectrum of the bright B-type star ϵ CMa.

In our nomenclature, on-axis (target) spectra are designated as type 1, off-axis (airglow) spectra as type 2, and spectra obtained through the tin filter as type 3. While the *ORFEUS-SPAS I* data set consists only of spectra A1, B1, C1, and D1, up to twelve separate spectra may be extracted from the *ORFEUS-SPAS II* data, three from each grating. In practice, however, we extract the airglow spectrum only from Grating D and the tin-filter spectrum only from Grating B, reducing the actual number of spectra to six: A1, B1, B3, C1, D1, and D2. Airglow spectra from Gratings A, B, and C are less useful than those from Grating D: the Grating A bandpass contains no geocoronal features, and spectrum B2 is contaminated by flux from spectrum A1. For most targets, spectrum C1 contains no astrophysical flux, so extracting an airglow spectrum is redundant. Complete photon lists for each detector, along with tools for extracting spectra from them, are available from the archive (see Section 3).

2.2. *Spectral Extraction*

Each photon event processed by our electronics requires 24 bits of encoding: 15 bits for the X (dispersion direction) coordinate, 8 bits for Y, and 1 bit for detector identification. The image size is thus $32,768 \times 256$ pixels. In the FUV (900–1200 Å), a single pixel in X corresponds to a

wavelength interval of approximately 0.014 Å. The instrumental resolution is ~ 0.23 Å, so the spectra are highly oversampled in wavelength. In the spatial domain, one X pixel corresponds to about $0''.3$ of sky, one Y pixel to about $10''$.

For the *ORFEUS-SPAS I* data set, we find that, at a given detector X coordinate, the FWHM of our spectra averages 5 pixels in the Y dimension. We thus sum the counts over 11 Y pixels (best-fit center ± 5 pixels), a range that encompasses more than 98% of the dispersed photon events. The general background is scaled from two strips, each spanning 3 pixels in Y, immediately above and below the spectral region of the detector. For the second mission, improvements in the detector electronics tightened the point-spread function in both dimensions. Accordingly, we use a 9-pixel window, with three pixels of background on either side, in our extraction of spectra obtained on *ORFEUS-SPAS II*.

Extraction windows were defined once for each spectrum and each flight. The spectra are not observed to drift out of the standard extraction windows during the *ORFEUS-SPAS I* mission, but move slightly during the first few days of the *ORFEUS-SPAS II* flight. We correct for these motions by shifting the standard extraction window by up to three pixels in Y. The motions are largest in the EUV spectra. Grating D spectra do not show significant motion except for one observing period (GMT day 330) during the *ORFEUS-SPAS II* mission. On this flight, the spacecraft was twice required to assume a "minimum drag" configuration, in which the platform orientation was held fixed relative to the ram vector. After the second minimum-drag episode, which lasted for 12 hours, thermal stresses in the spacecraft resulted in a significant shift in the position of the spectrum on the detector, requiring a re-definition of the extraction window for observations in this time frame. The data quality does not seem to have been compromised. The minimum-drag event and its consequences are discussed in Hurwitz et al. (1998).

For each observation, a photon-event list is extracted from the spacecraft data stream. A preliminary extraction of the FUV spectrum (if available and sufficiently bright) is used to produce a plot of count rate versus integration time. These plots are manually inspected, and "good times" (target in aperture, background rate low, telemetry uninterrupted, etc.) are identified. Status information from the spacecraft star tracker is used to establish good times when spectrograph data cannot. Only data from

these good times are included in the photon-event lists and extracted spectra that are supplied to the data archives. Users interested in time-series analyses should determine whether time segments have been excluded from the observation of interest.

2.3. *Dead Time and Gain Sag*

When the spectral photon-event rate approaches the capacity of the telemetry system (about 4400 events s^{-1}), instrument dead-time effects become important. The detector electronics create "stimulation" events (or stim pins) at the detector edges at a rate ($\sim$ 2 s^{-1}) that can be measured during slews and other quiet periods. The observed rate of these events during on-target pointings enables us to estimate the dead time for genuine spectral photons. Data buffering and the non-periodic nature of the telemetry-sampling system ensure that the throughput for both stimulation and actual photon events is identical.

When the current flow parallel to the microchannel plate surface cannot replenish the electrons being drained from the channel walls, the modal gain may sag. Gain sag is a function of local count rate caused by unusually bright emission-line or continuum targets and must therefore be distinguished from overall dead-time effects, which are a function of total count rate, including background. Gain sag is of greatest concern near the center of the band, where the astigmatism or spectral height is minimized. In the Y-dimension, gain sag causes a loss of spatial resolution, with the result that some source events are not contained within the nominal extraction window. (Spectral spillover unrelated to gain sag may also occur if the source falls very near the edge of the entrance aperture.) The remedy is to study the extracted background spectra for evidence of spectral spillover and to adjust the background-subtraction procedure accordingly.

The delay-line system that calculates the photon X coordinate is generally robust against gain sag, but high local count rates can lead to wavelength-dependent variations in throughput. A very bright continuum source may suffer an uncorrected loss of throughput over broad regions in which the astigmatism is small. We find a depression of the observed continuum whenever the local flux exceeds approximately 5×10^{-11} erg cm^{-2} s^{-1} Å^{-1} for wavelengths less than about 1110 Å. At longer wavelengths, instrumental astigmatism broadens the spectrum in Y, reducing the local count rate. In addition, spurious absorption features can be observed at approximately 1047, 1052.5, 1057, and 1060 Å. We have determined that these features are fixed in detector coordinates, but may vary somewhat in their assigned wavelengths. For each spectrum that exceeds this brightness limit, warnings have been placed in the corresponding file headers.

2.4. *Pointing Effects*

For fine pointing, the spacecraft's attitude control system (ACS) utilizes signals from a star tracker aligned with the ORFEUS telescope axis. Under normal circumstances, the ACS achieves an absolute pointing error of less than $\sim 5''$. For a few targets, plots of count rate versus time clearly indicate that the target was not centered in the aperture but fell near the edge; the spectra obtained during these pointings are labeled (in both the file headers and published catalogs) as non-photometric. Pointing jitter was about $\pm 2''$ peak to peak on both flights of the ORFEUS telescope. No attempt has been made to correct our spectra for the motion of the target in the aperture.

Because the telescope and star tracker were aligned using BEFS Grating D spectra, any defocus in the telescope (relative to the aperture plane of the spectrograph) would cause light destined for the other gratings to be displaced systematically toward the aperture edge. We believe that some spectra obtained with Gratings A and B on the *ORFEUS-SPAS II* mission suffer partial occultation, both because variations in the measured flux are greater than we can otherwise account for, and because sources observed with Grating B through the much larger tin-filter aperture do not show flux variations. Because the occultation effects cannot be calculated *a priori*, BEFS EUV spectra must be treated as non-photometric.

2.5. *Backgrounds*

The on-orbit background event rate, measured on an unilluminated region of the FUV detector during a night-time observation, is about 0.0016 counts per second per resolution element (9 pixels in Y by 25 in X), due mostly to detector dark counts and cosmic rays. The rate measured in an extracted spectrum far from any airglow feature ranges from about 0.003 s^{-1} at night to 0.04 s^{-1} in some daytime pointings, probably due to stray Lyman α radiation. (The daytime rate of 0.0044 s^{-1} quoted in Hurwitz et al. 1998 is a typographical error.)

The day and night count rates in the "bright corner," a region of enhanced background flux present on both detectors on both missions (see Fig. 2), are approximately 0.09 and 0.01 s^{-1}, respectively. Their ratio corresponds roughly to the day/night intensity ratio of diffuse Lyman α emission. In the 1993 data set, the bright corner contaminates Grating A spectra at wavelengths shorter than about 420 Å and Grating D spectra shorter than about 960 Å. In the 1996 data set, Grating D spectra are contaminated at wavelengths below about 1000 Å, while the accidental shift of Grating A moved its spectrum away from the bright corner.

After the *ORFEUS-SPAS I* mission, substantial baffling was added to the ORFEUS Echelle Spectrometer (Barnstedt et al. 1999) with which the telescope was shared. It was expected that this baffling would eliminate the bright corners on the Berkeley detectors. The effect, however, is essentially unchanged in the *ORFEUS-SPAS II* data set and has since been attributed to a zero-order reflection from the Berkeley gratings of a light leak at a hardware interface seam.

The irregular footprint of the bright corner creates a crossover region in our FUV spectra (Grating D) within which the background cannot simply be scaled from the 3-pixel strips above and below the spectrum. To estimate the background here, we assume that the shape of the background in the spectral region and in the adjacent strips differs only by a translation in the X coordinate, determined from detector images collected during slew periods. The process is illustrated in Fig. 3, which shows part of an airglow spectrum obtained on the *ORFEUS-SPAS II* mission. To model the background between 965 and and 1022 Å, we shift the background spectra extracted

from the regions above (BG1) and below (BG0) the target spectrum by 600 pixels in X (~ 8.6 Å; BG1 is shifted to the left, BG0 to the right), then scale their sum to the width of the target extraction window. For the *ORFEUS-SPAS I* dataset, we shift the background strips by ± 750 pixels in X (~ 10.7 Å) in the region between 920 and 977 Å. It is possible for this procedure to introduce artificial features within the overlap region. Artifacts of this type are not expected to be as narrow as unresolved spectral features, nor are they likely to exceed 10% of the background in amplitude. As such, they are of potential concern only for very faint targets.

The extraction of Grating A spectra is complicated by two effects. On the 1993 flight, wavelengths shorter than about 420 Å are contaminated by the bright corner. The background in the crossover region (about 390–420 Å) is estimated as for the Grating D spectra, and the same caveats apply. On the 1996 flight, the Grating A spectra moved away from the bright corner, but were left crossing the Grating B spectra, contaminating spectrum A1 between 400 and 460 Å and spectrum B1 between 550 and 590 Å. We have developed an algorithm to estimate the contamination of spectrum A1 by shifting and adding the background strips (similar to the scheme used for the edge of the bright corner), but the resulting background array provides only a rough estimate of the contamination due to spectrum B1. Researchers interested in absorption features or other spectral details should consult the raw-counts spectra, which are not background subtracted, to confirm the reality of apparent spectral features in this band. The higher effective area of Grating B (Section 2.7.2) makes the contribution of the overlap to spectrum B much less significant, and we do not attempt to correct for it.

2.6. *Spectral Resolution and Wavelength Scale*

The BEFS monochromatic point-spread function (PSF) is determined by fitting Gaussian line profiles to emission features in the spectrum of the bright symbiotic binary RR Tel. Penston et al. (1983) list the mean line width for each emitting species, determined from high-resolution *IUE* spectra. Assuming that the intrinsic line width and instrument resolution add in quadrature, Hurwitz et al. (1998) derive independent PSF values from the lines of eight emitting species and quote a mean instrumental resolution of ~ 95 km s^{-1} for the BEFS spectrograph. We have repeated this analysis using our re-extracted spectra and the updated line list presented in Table 2. (Line identifications were kindly provided by Brian Espey.) Emission lines from nine species listed in Penston et al. are present in the BEFS spectrum of RR Tel. Their intrinsic (*IUE*) widths range from 43 to 78 km s^{-1} (FWHM), and their measured (BEFS) widths from 79 to 187 km s^{-1} (FWHM). The resulting PSF values range from 63 to 175 km s^{-1}. While our results are similar to those of Hurwitz et al., we note that six of the nine species yield PSF values between 60 and 70 km s^{-1}. RR Tel is a dynamic system, and the three high values, from He II, C IV, and O IV, may well reflect changes in the intrinsic widths of these lines over the decade between the *IUE* and BEFS observations. Rejecting the three high values, we average the remaining six to find a mean instrumental PSF of

TABLE 2
EMISSION FEATURES IN THE SPECTRUM OF RR TEL

Feature	λ_{lab} (Å)	Feature	λ_{lab} (Å)
S VI	933.38	O IV	1067.81
He II	942.51	S IV	1072.97
S VI	944.52	N II	1083.99
He II	949.33	He II	1084.94
He II	958.70	P II	1124.95
C III	977.02	Ne V]	1136.66
Ne VI]	997.40	Ne V]	1145.83
Ne VI]	999.63	P II	1152.83
Ne VI]	1006.10	C IV	1168.94
Ne VI]	1010.60	Mg VI]	1190.07
O VI	1031.93	Mg VI]	1191.64
O VI	1037.62	S V	1199.18
S IV	1062.66	Si III	1206.51

NOTE.— This set of lines differs slightly from that used to define the BEFS wavelength scale (shown in Fig. 4); it has been revised to reflect recent results.

~ 66 km s^{-1}, or 0.23 Å. This result is consistent with both preflight laboratory measurements of the BEFS resolution (Hurwitz et al. 1998) and recent analyses of interstellar molecular-hydrogen absorption-line spectra (Dixon et al. 2001).

Over most of the FUV bandpass, the relationship between the observed wavelength and the detector X coordinate is well modeled by a linear function of X plus a smooth departure that does not exceed ± 0.13 Å. This departure from linearity, derived from an optical ray trace of the telescope and spectrograph, is presented in Fig. 4. The ray trace provides the shape of this curve, but not its absolute position in wavelength space. We have thus shifted the curve to best reproduce the measured positions of emission lines in the spectrum of RR Tel, also plotted in Fig. 4. In two wavelength regions, 990–1010 and 1125–1145 Å, the line positions in the RR Tel spectrum show significant deviations from our ray-trace predictions. In the end, we decided not to model these deviations, but instead exclude these regions when fitting our model curve to the RR Tel line positions. We supplement the wavelength solution at short wavelengths with Lyman-series absorption lines in several white-dwarf stars and at long wavelengths with emission features from the late-type star α CMi.

Temporal changes in the FUV wavelength scale, seen on both flights, are modeled with a time-dependent offset and a linear stretch. We combine repeated observations of diffuse emission (airglow) lines and RR Tel to characterize these effects. (RR Tel was observed only once on the *ORFEUS-SPAS I* mission.) This new wavelength calibration represents a significant improvement over those initially provided with the *ORFEUS-SPAS I* data set, which suffered from significant non-linearities, and the *ORFEUS-SPAS II* spectra, which were poorly constrained at the longest wavelengths. To establish a wavelength scale for the off-axis aperture, we apply a fixed offset, determined from the average of the strongest diffuse emission features, to the on-axis wavelength solution.

The EUV wavelength scale is derived from pre-flight laboratory measurements. For spectra B and C, the airglow features He I $\lambda 584.33$ and O II $\lambda\lambda 832.8$–834.5 (respec-

tively) provide a fixed point for the wavelength calibration and a measure of its temporal drift. Because spectrum A contains no measurable emission features, its wavelength calibration is considerably more uncertain.

The wavelengths assigned by our spectral-extraction software reflect the effects mentioned above, as well as spectral shifts due to anomalous thermal conditions following the second minimum-drag period on the *ORFEUS-SPAS II* mission. Relative wavelength errors within a given spectrum should be less than ~ 0.2 Å between 915 and 1216 Å. (The *ORFEUS-SPAS I* spectra extend only to 1175 Å.) Because of the unknown placement of each target within the aperture, an overall offset of ± 0.5 Å may exist in any individual FUV spectrum.

2.7. *Flux Calibration*

Flux calibration of the BEFS is based on in-flight observations of hot DA white dwarfs. The efficacy of this method for on-orbit calibration in the FUV has been demonstrated by Kruk et al. (1997, 1999). Our principal calibration stars are G 191–B2B for the *ORFEUS-SPAS I* data set and HZ 43 for *ORFEUS-SPAS II*. Given the uncertainties in the model atmospheres and synthetic spectra, the adopted stellar V magnitudes and temperatures, and the photometric accuracy and background subtraction of the extracted count-rate spectra, we quote an uncertainty in the BEFS flux calibration of $\lesssim 10\%$.

2.7.1. *ORFEUS-SPAS I*

Vennes et al. (1996) model the FUV spectrum of G 191–B2B obtained on the *ORFEUS-SPAS I* mission. Following them, we use the pure-hydrogen models of Vennes (1992) and adopt the stellar parameters $T_{\mathrm{eff}} = 60,000$ K, $\log g = 7.535$, and $V = 11.781$. T_{eff} and $\log g$ represent an average of the maximum and minimum values found in the literature (Bergeron et al. 1994; Finley et al. 1997; Marsh et al. 1997; Vennes et al. 1997) and are in excellent agreement with those used by Bohlin et al. (1995) and Kruk et al. (1997) to flux-calibrate the *Hubble Space Telescope* / Faint Object Spectrograph (FOS) and Hopkins Ultraviolet Telescope (HUT), respectively. The V magnitude is taken from the compilation of Bohlin et al. (1995). We scale the model by the H I interstellar opacity, adopting a column density of $\log N(\mathrm{H\ I}) = 18.31 \pm 0.01$ (Dupuis et al. 1995), a value consistent with the recent *HST* result of Vidal-Madjar et al. (1998), and add a synthetic second-order spectrum scaled to the observed flux between 865 and 912 Å. (The ratio of second- to first-order counts in the BEFS FUV spectrum of G 191–B2B is ~ 0.02.) The model is then convolved with the instrument-resolution profile. An effective-area curve is derived by dividing the count-rate spectrum of G 191–B2B by the final synthetic stellar spectrum. The result is fitted with a fifth-order Legendre polynomial to remove structure on small spatial scales.

G 191–B2B was observed four times on the *ORFEUS-SPAS I* mission. We use three other stars, MCT 0501–2858, MCT 0455–2812, and HD 220172, as transfer standards to establish effective-area curves for the first and final days of the mission. The resulting family of effective-area curves is shown in Fig. 5. Effective-area curves for

Gratings A and B are derived from observations of G 191–B2B in the same way as for Grating D. The differences among the Grating A effective-area curves appear to be real and indicate a decrease in sensitivity with time, especially at long wavelengths. The differences among the Grating B curves, however, are not significant given the signal-to-noise ratios of the individual spectra. We thus average the four curves shown into a single effective-area curve for this spectrum. Our Grating C spectrum of G 191–B2B exhibits no significant first-order astrophysical flux; we adopt a theoretical effective-area curve for this spectrum.

FUV spectra of hot stars with low H I column densities are contaminated by stellar EUV flux in second order. For each such star, we use spectra A and B to compute the second-order contribution to spectra C and D, scaling a theoretical second-order effective-area curve to match the raw counts observed in spectrum C and in spectrum D below 912 Å. The resulting second-order spectra are provided for users who wish to subtract the second-order contribution to their FUV spectra. Figure 5 shows a number of second-order curves for spectrum C. The highest represents the effective area through the first half of the 1993 flight; we apply an average of the remaining curves to observations obtained in the second half.

2.7.2. *ORFEUS-SPAS II*

The flux calibration for *ORFEUS-SPAS II* is based on observations of HZ 43 as described in Hurwitz et al. (1998). We have repeated that calculation, but include a correction for the second-order contribution to the observed FUV spectrum that was neglected in the earlier analysis. We use the white-dwarf models of Vennes (1992), adopting the stellar parameters $T_{\mathrm{eff}} = 50,000$ K and $\log g = 8.0$. These parameters were used by Bohlin et al. (1995) for the flux calibration of the FOS and agree with published values (e.g., Napiwotzki et al. 1993). We normalize the model to the star's visual magnitude ($V = 12.914$; Bohlin et al. 1995) and scale by the interstellar hydrogen opacity, assuming a column density of $\log N(\mathrm{H\ I}) = 17.94 \pm 0.03$ (Dupuis et al. 1995). We add the synthetic first- and second-order spectra and convolve the result with the instrument-resolution profile to obtain a model stellar spectrum. To derive the first-order effective-area curve, we divide the count-rate spectrum of HZ 43 by this synthetic spectrum and fit the result with a fifth-order Legendre polynomial to retain the overall shape of the curve while removing structure on small spatial scales.

Because Grating D was shifted to longer wavelengths for the 1996 mission, it does not sample enough of the wavelength region shortward of 912 Å to constrain models of the second-order stellar spectrum. Instead, we derive the instrument's second-order effective-area curve using laboratory data for the mirror and grating reflectivity, detector quantum efficiency, and grating efficiency, then scale the result (slightly) to match the observed second-order He I $\lambda 584$ geocoronal line. A synthetic EUV spectrum of HZ 43 is multiplied by the computed second-order effective area to model the star's second-order contribution at FUV wavelengths. We find that the ratio of second- to first-order counts in the BEFS FUV spectrum of HZ 43 rises from 0.01 to 0.04 between 1000 and 1200 Å.

The helium white dwarf MCT 0501–2858 is used as a transfer standard to establish effective-area curves for the first and final days of the mission. Because we lack a reliable EUV model for this star, we use a spectrum observed by the *Extreme Ultraviolet Explorer (EUVE)* to estimate its second-order flux. The complete family of effective-area curves is shown in Fig. 6.

In our assignment of effective-area curves to individual FUV spectra, we interpolate linearly with time among the flux-calibration files for the *ORFEUS-SPAS I* data set, as these vary smoothly through the mission. During the *ORFEUS-SPAS II* mission, the effective area changes dramatically over the first two days of the mission, but remains stable thereafter (Fig. 6). We thus assign specific effective-area curves to observations taken during each of the first two observing shifts and use the mean of all subsequent curves to calibrate spectra for the rest of the mission, as described in Hurwitz et al. (1998).

On *ORFEUS-SPAS II*, the effective area of the FUV channel falls early in the mission, then rises and remains nearly constant for the remainder of the 14-day flight. Presumably, this reflects condensation and evaporation of outgassed material onto the optics. The effective area falls throughout the five-day *ORFEUS-SPAS I* mission. The behavior differs between the two missions, we believe, because the first flight was the maiden voyage of the *ASTRO-SPAS* spacecraft and thus subject to a higher level of contamination. (A second, two-week flight of *ASTRO-SPAS*, with another payload, took place between the two *ORFEUS-SPAS* missions.)

The long-wavelength dip in the effective area apparent early in both missions reflects, we believe, variations in the "pulse height" or amplitude of the charge cloud reaching the detector caused by adsorption of molecules onto the microchannel plate (MCP) during integration. Subsequent "scrubbing" of the MCP during observations on orbit desorbs the molecules, restoring the original MCP gain. We cannot test this hypothesis directly, because pulse-height information is not included in the *ORFEUS-SPAS* flight telemetry stream. Preflight measurements, however, indicate higher-than-average gain in the region of the detector that subsequently shows a dip in effective area. We therefore suspect a pulse-height effect.

Comparison of the *ORFEUS-SPAS I* and *II* effective-area curves reveals a dramatic increase in the spectrograph's FUV sensitivity from the first flight to the second. In preparation for the second flight, the two long-wavelength diffraction gratings were over-coated with silicon carbide, increasing their reflectivity at FUV wavelengths. The effective area of our Grating B spectra is essentially unchanged from one flight to the next, but the Grating A sensitivity is reduced by half. For both channels, the effective area falls precipitously for the first few days of the mission. In fact, it is likely that the sensitivity of our detector was fairly stable, but that EUV observations of HZ 43, our flux-calibration target, suffered the photometric problems described in Section 2.4. Rather than attempting to correct individual spectra for this effect (which may differ greatly from one target to another), we have used a single flux-calibration file, obtained early in the mission, for each of the Grating A and B spectra obtained on the *ORFEUS-SPAS II* mission. The absolute flux calibration of these spectra is therefore suspect.

The tin filter, unavailable on the 1993 flight, was used in 1996 for observations of the bright B-type star ϵ CMa and two flux-calibration sources, HZ 43 and MCT 0501-2858. The ϵ CMa spectra were published (Cohen et al. 1998) before the tin-filter effective-area curve (plotted in Fig. 6) became available. Observations obtained through the tin filter appear not to suffer the flux losses seen in the other EUV data sets, perhaps because the aperture containing this filter is much larger than the standard observing aperture.

Because our primary flux-calibration star for the *ORFEUS-SPAS I* mission, G 191–B2B, shows no flux in the wavelength range covered by spectrum C, we used a theoretical effective-area curve for the Grating C spectra from that flight. The *ORFEUS-SPAS II* calibration target HZ 43 has a lower H I column and exhibits enough flux at short wavelengths (670–720 Å) that we were able to scale the theoretical effective-area curve to the observed intensity.

Second-order effective-area curves for Gratings C and D were derived theoretically, as described above, then scaled to reproduce the sub-Lyman-limit flux at the long-wavelength end of spectrum C and the He I λ584 geocoronal line in spectrum D, respectively. Because of the photometric problems apparent in our EUV data, it is possible that an EUV-emitting source could contribute second-order flux to a Grating D spectrum that is not accounted for in the corresponding Grating A and B spectra. Users should thus take care when subtracting the second-order spectra provided with the *ORFEUS-SPAS II* data.

2.8. *Flat-Field and Other Effects*

Hurwitz et al. (1998) discuss the statistical distribution of fluctuations in the response of the BEFS detector to uniform illumination. We examine two types of flat-field effects in Fig. 7, which presents four spectra of HZ 43 obtained over the course of the *ORFEUS-SPAS II* mission. The spectra are plotted in pixel space; the wavelength scale is approximate. Note the four narrow, P Cygni-like features at about 1036, 1042, 1047, and 1053 Å. These features are nearly fixed on the detector, but vary somewhat in wavelength space. They are not seen in most BEFS spectra, which have lower signal-to-noise ratios. In much brighter targets, these are the locations of the spurious absorption features discussed in Section 2.3; the two effects are likely to be related. At shorter wavelengths, Fig. 7 shows a broad trough in the spectral continuum between about 990 and 1000 Å. Early in the mission (bottom curve), the feature has sharp edges and a flat core; later, the drop becomes more gentle and the feature considerably less prominent. We do not attempt to correct for flat-field effects in the BEFS spectra.

The reader is referred to Hurwitz et al. (1998) for further discussion of the detector background and flat field, grating scatter within the plane of dispersion, and the use of spectra obtained through the off-axis aperture to estimate the contribution of diffuse airglow emission.

3. THE DATA SET

BEFS data from both the *ORFEUS-SPAS I* and *II* missions are available from the Multimission Archive at

STScI (MAST; http://archive.stsci.edu/mast.html). All files are in FITS format, with the data stored as one or more binary-table extensions. The data-reduction procedures employed to produce these files may be summarized as follows:

1. Accumulate data between designated start and stop times. Identify "good times." Produce a photon-event file, which lists position and arrival time *(x, y, t)* for each event on a given detector, including stim pins. Only events which arrive during good times are included in the photon-event file. This step is applied independently to the data stream for each observation and each detector.

2. Extract photon events from the desired aperture, its associated background regions, and the nearest stim pin. Extraction windows are predefined and are constant throughout each mission, except as discussed in Section 2.2.

3. Determine detector dead time from stim-pin counts and exposure time.

4. Correct the wavelength scale for temporal effects (a stretch and shift).

5. Convert the photon-event list into a raw-counts spectrum. Combine the background strips and scale to produce a background spectrum. Smooth the background array by 13 pixels (~ 0.18 Å). Generate error arrays (assuming Gaussian statistics) for both the target and background spectra.

6. Apply the flux calibration as follows: `FLUX_PHOT = (SPEC - BKGD)` $\times$ `DT_CORR / (EFF_AREA` $\times$ `EXPTIME` $\times$ `DELTA_WAV)`, where `FLUX_PHOT` is the flux-calibrated spectrum in units of photons cm^{-2} s^{-1} Å^{-1}, `SPEC` and `BKGD` are the raw-counts and background arrays, `DT_CORR` is the dead-time correction, `EFF_AREA` the effective area in cm^2, `EXPTIME` the exposure time in s, and `DELTA_WAV` the width of a pixel in Ångstroms.

7. Write out the fully-calibrated spectrum as a FITS binary table extension according to the format presented in Table 3.

Steps 2–7 are performed independently for each aperture. We do not attempt to correct BEFS spectra for detector flat-field effects, photometric losses due to miscentering of the target in the aperture, or resolution degradation resulting from pointing jitter. We provide, but do not subtract, FUV airglow (D2) spectra obtained on the 1996 mission. (Because the D1 and D2 spectra have different point-spread functions, one cannot simply be subtracted from the other.)

8. Model the second-order contribution to the FUV spectrum and write it to a second binary table extension in the SPD1 file, using the format given in Table 3. The units of the second-order spectrum are raw counts; gaps in the data are set to zero. To apply the correction, smooth the second-order array and subtract it from the first-order raw-counts spectrum. Re-calibrate the first-order spectrum using the recipe given in Step 6. Photometric uncertainties or spectral anomalies in the second-order spectra (especially for the *ORFEUS-SPAS II* data) may require manual intervention. This step is performed only on data sets for which EUV spectra are available.

The complete set of software used to extract and calibrate BEFS spectra (written in C), together with all supporting parameter and calibration files, are available from MAST. In addition, we have written two IDL routines to manipulate BEFS data. The first, makeair.pro, reads an airglow (D2) file and scales a synthetic airglow spectrum to the observed line intensities. The second, extract_tt.pro (also available in C), reads a photon-event file (LST1) and returns the detector X coordinate and arrival time of each photon falling within a user-defined region of the detector. General IDL routines to read and manipulate BEFS data files are available from the IDL Astronomy User's Library (http://idlastro.gsfc.nasa.gov).

4. DISCUSSION

The various instrumental and detector effects discussed above are best appreciated by an examination of the data. Figure 8 presents the complete spectrum of G 191–B2B obtained on the *ORFEUS-SPAS I* flight of BEFS. It is

TABLE 3
BEFS FILE FORMATS

Field Name	Units	Description
First-Order Spectra		
WAVELENGTH	Å	Wavelength array
FLUX_PHOT	photons cm^{-2} s^{-1} Å^{-1}	Calibrated flux in photon units
FLUX_ERGS	erg cm^{-2} s^{-1} Å^{-1}	Calibrated flux in energy units
FRAC_ERR	$\cdots$	Fractional uncertainty in the flux (1 σ)
X	pixels	Pixel number
SPEC	counts	Extracted spectrum
BG0	counts	Spectrum of background region 0
BG1	counts	Spectrum of background region 1
BACKGROUND	counts	Normalized background, smoothed by 13 pixels
BG_ERR	counts	Uncertainty in the background (1 σ)
DELTAW	Å	Wavelength increment
EFF_AREA	cm^{-2}	Effective area
Second-Order Spectra		
WAVELENGTH	Å	Wavelength array
2ND_COUNTS	counts	Estimated second-order spectrum
2ND_SIGMA	counts	Uncertainty in second-order spectrum (1 σ)
2ND_AEFF	cm^{-2}	Second-order effective area

the sum of four individual pointings with a total integration time of 8100 s. The individual spectra from Gratings B and D, which have well-defined spectral features, were cross-correlated before being combined.

Note the low signal-to-noise ratio at the shortest wavelengths, where the strong background flux of the bright corner has been subtracted from spectrum A. The He I edge at 504 Å is just visible at the long-wavelength end of this spectrum. Spectrum B shows a steep drop in the continuum flux toward long wavelengths, punctuated by the geocoronal He I $\lambda584$ line. Because the interstellar medium toward G 191–B2B is nearly opaque at wavelengths between 650 and 912 Å, spectrum C is dominated by second-order EUV emission. The apparent peak at ~ 750 Å reflects a dip in the first-order flux-calibration curve (Fig. 5) applied by our calibration software. The geocoronal O II $\lambda\lambda832.8$–834.5 multiplet is weak in this spectrum. Flux from the bright corner has been subtracted from the short-wavelength end of spectrum D, but does not significantly affect the signal-to-noise ratio of this bright FUV source. The BEFS FUV spectra of G 191–B2B are analyzed by Hurwitz & Bowyer (1995) and Vennes et al. (1996).

Figure 9 shows the spectrum of HZ 43 obtained on the *ORFEUS-SPAS II* mission. Six individual observations, totaling 8700 s, were combined to make this plot. Because some of the EUV spectra in this data set are non-photometric, the individual flux-calibrated spectra were weighted by their continuum flux, integrated over a selected wavelength region, before being summed. The final spectrum was then rescaled to the intensity of the initial HZ 43 observation, which for spectra A and B is significantly brighter than subsequent observations. The time-dependent stretch and shift in the BEFS wavelength scale is particularly apparent in these data, which span the entire two-week mission. Individual spectra were cross-correlated before being combined. Spectrum D was cross-correlated twice, once using only the Lyman γ $\lambda973$ line, and again using only the short-wavelength wing of the Lyman α $\lambda1216$ line. The resulting spectra were spliced together at 1050 Å. For scientific analysis, a better approach would be to re-sample all six spectra onto a uniform wavelength grid.

Spectrum A is no longer contaminated by the bright corner, but its overlap with the Grating B spectra severely complicates the region between 400 and 460 Å. Our software attempts to model and subtract this contamination, but is not entirely successful; for example, the strong emission features seen in this region are actually geocoronal He I lines from spectra B1 and B2 (see Fig. 2). The He I edge at 504 Å is present in both spectra A and B, and the lower neutral-hydrogen column density toward HZ 43 allows first-order flux to reach us at the short-wavelength end of spectrum C. The bright FUV spectrum of HZ 43 is relatively immune to the bright corner, but its high signal-to-noise ratio highlights a number of flat-field effects, as discussed in Section 2.8. Also apparent are the diffuse emission features of O I $\lambda989$, Lyman β $\lambda1026$, and He I $\lambda584$ in second order. The BEFS FUV observations of HZ 43 are analyzed by Dupuis et al. (1998).

BEFS, the Berkeley Extreme and Far-Ultraviolet Spectrometer, offers a unique combination of spectral resolution and effective area in the comparatively unexplored FUV wavelength band. We are pleased to make the entire BEFS data set available to the community in a standard (FITS) format with improved flux and wavelength calibrations.

REFERENCES

Barnstedt, J. et al. 1999, A&AS, 134, 561
Bergeron, P., Wesemael, F., Beauchamp, A., Wood, M. A., Lamontagne, R., Fontaine, G., & Liebert, J. 1994, ApJ, 432, 305
Bohlin, R. C., Colina, L., & Finley, D. S. 1995, AJ, 110, 1316
Cohen, D. H., Hurwitz, M., Cassinelli, J. P., & Bowyer, S. 1998, ApJ, 500, L51
Dixon, W. V., Hurwitz, M., & Lee, D.-H. 2001, ApJ, submitted
Dupuis, J., Vennes, S., Bowyer, S., Pradhan, A. K., & Thejll, P. 1995, ApJ, 455, 574
Dupuis, J., Vennes, S., Chayer, P., Hurwitz, M., & Bowyer, S. 1998, ApJ, 500, L45
Finley, D. S., Koester, D., & Basri, G. 1997, ApJ, 488, 375
Grewing, M. et al. 1991, in Extreme Ultraviolet Astronomy, ed. R. F. Malina & S. Bowyer (Elmsford: Pergamon), 437
Hurwitz, M. & Bowyer, S. 1986, Proc. SPIE, 627, 375
—. 1995, ApJ, 446, 812
Hurwitz, M. & Bowyer, S. 1996, in IAU Colloq. 152, Astrophysics in the Extreme Ultraviolet, ed. S. Bowyer & R. F. Malina (Dordrecht: Kluwer), 601
Hurwitz, M. et al. 1998, ApJ, 500, L1
Kruk, J. W., Brown, T. M., Davidsen, A. F., Espey, B. R., Finley, D. S., & Kriss, G. A. 1999, ApJS, 122, 299
Kruk, J. W., Kimble, R. A., Buss, Jr., R. H., Davidsen, A. F., Durrance, S. T., Finley, D. S., Holberg, J. B., & Kriss, G. A. 1997, ApJ, 482, 546
Marsh, M. C. et al. 1997, MNRAS, 286, 369
Napiwotzki, R., Barstow, M. A., Fleming, T., Holweger, H., Jordan, S., & Werner, K. 1993, A&A, 278, 478
Penston, M. V. et al. 1983, MNRAS, 202, 833
Vennes, S. 1992, ApJ, 390, 590
Vennes, S., Chayer, P., Hurwitz, M., & Bowyer, S. 1996, ApJ, 468, 898
Vennes, S., Thejll, P. A., Galvan, R. G., & Dupuis, J. 1997, ApJ, 480, 714
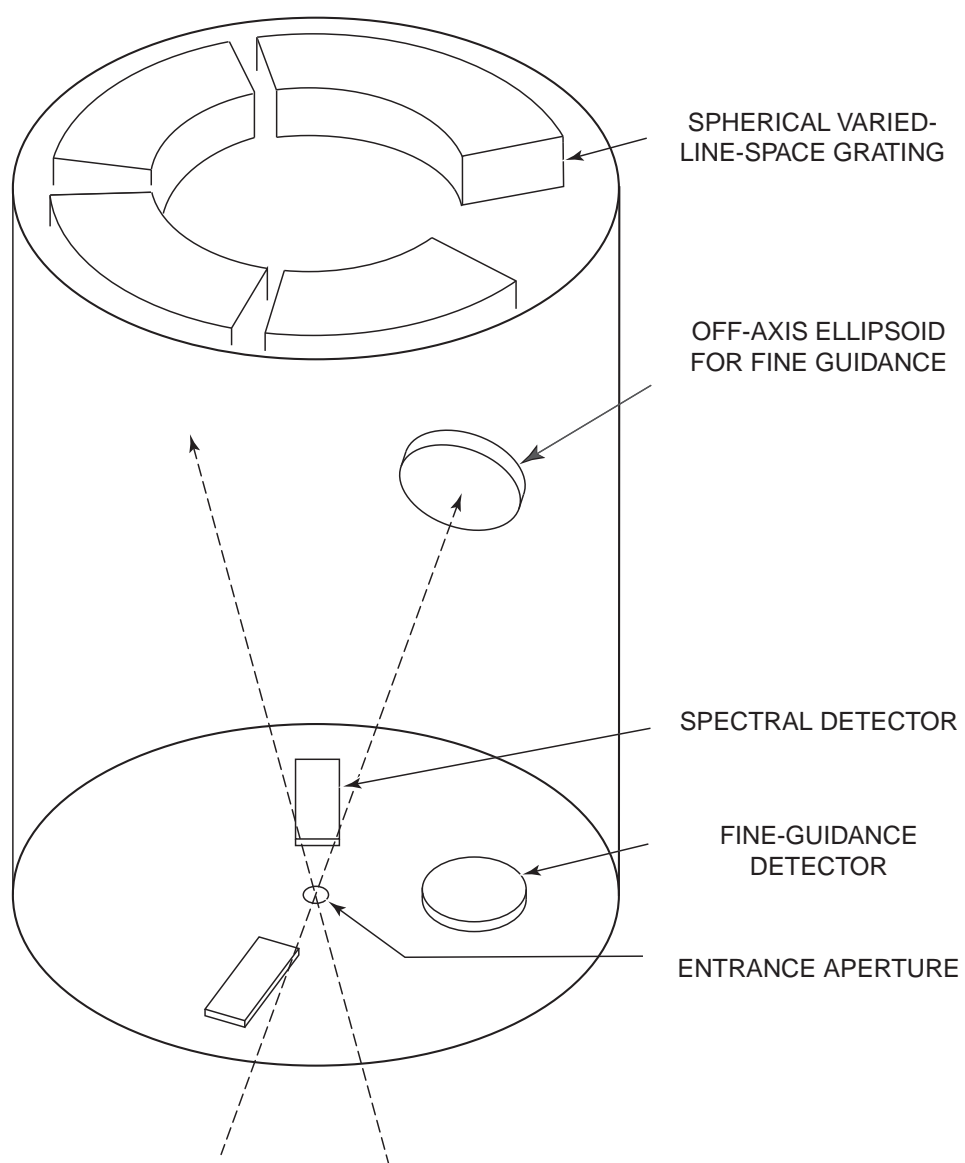Vidal-Madjar, A. et al. 1998, A&A, 338, 694

FIG. 1.— Schematic layout of the BEFS. The spectrograph entrance aperture lies at the focal point of the telescope.
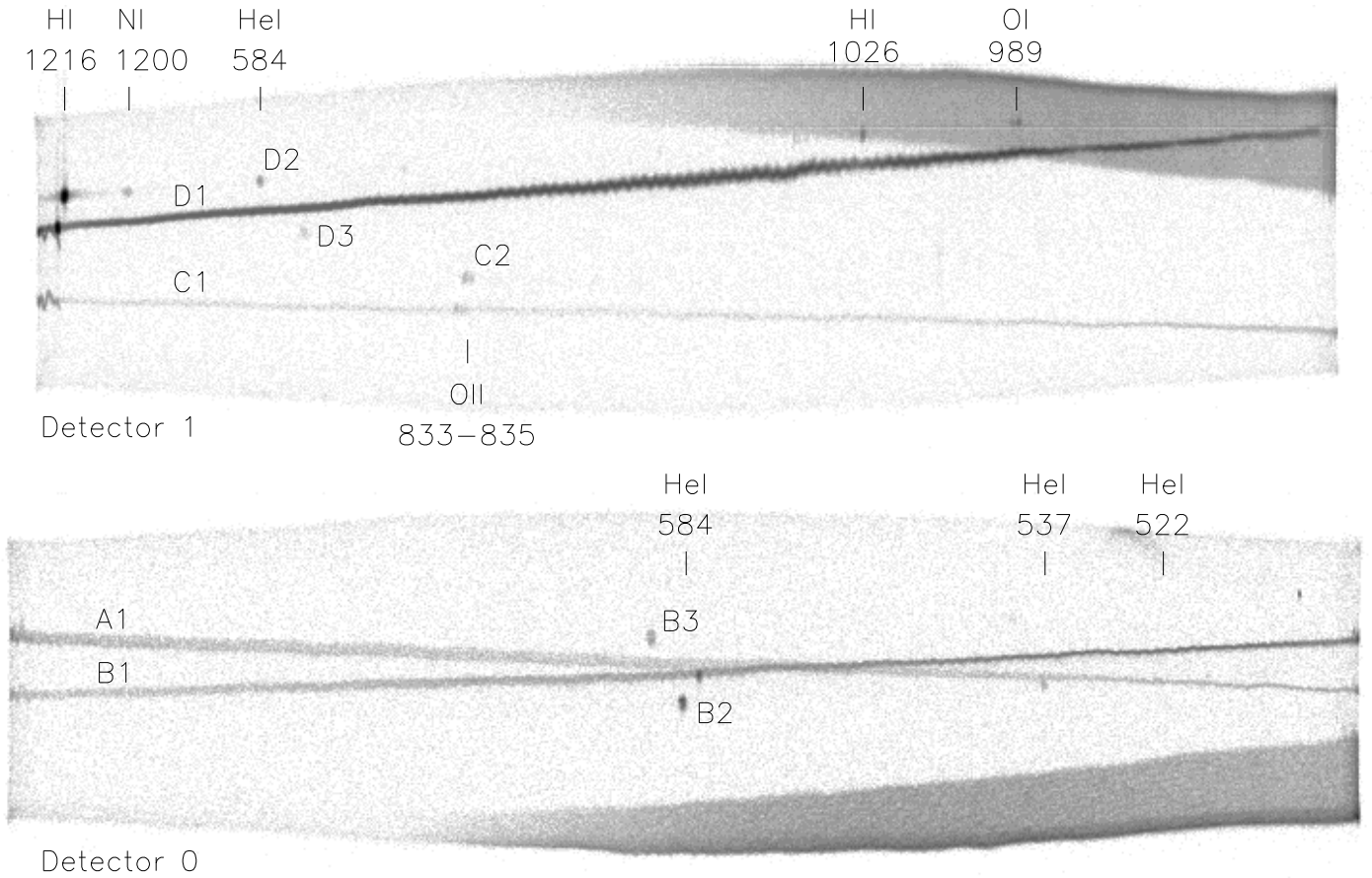
FIG. 2.— Logarithmically-scaled image of Detectors 1 (top) and 0 (bottom) for an observation of HZ 43 obtained on the *ORFEUS-SPAS II* mission. The continuum spectra, A1, B1, C1, and D1, are labeled, as are individual geocoronal lines in the off-axis B2, B3, C2, D2, and D3 spectra. (The B2 and D3 spectra were never extracted.) Selected emission features are labeled; note that wavelength increases to the left. The Grating A and B spectra cross on Detector 0. Note the bright corners on both detectors.
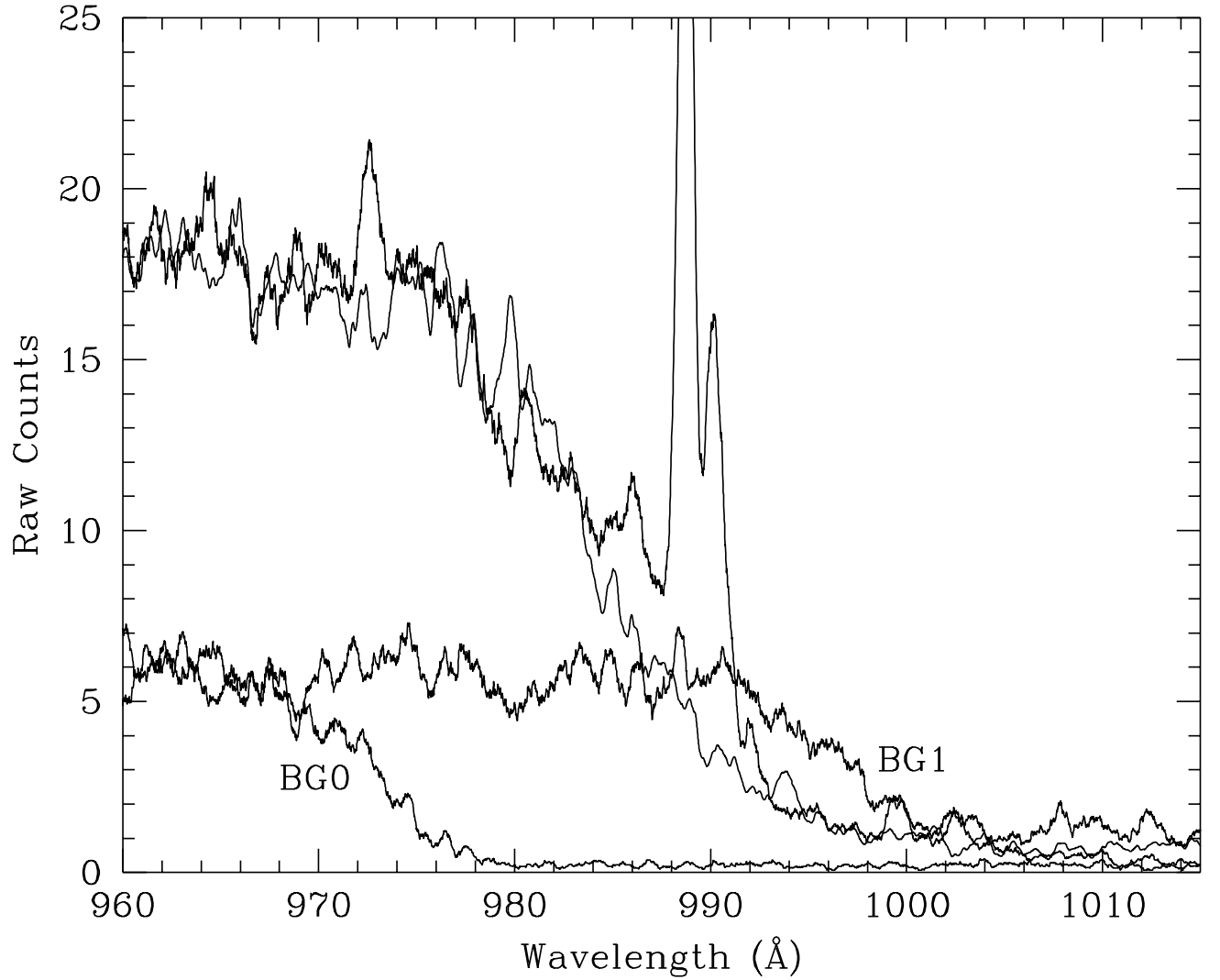
Fig. 3.— The edge of the bright corner seen in an *ORFEUS-SPAS II* airglow spectrum and its associated background spectra. In this region, the background cannot simply be scaled from the sum of the 3-pixel background strips above (BG1) and below (BG0) the target spectrum. Instead, we shift both spectra by 600 pixels in X ($\sim$ 8.6 Å), then sum and scale them to the width of the extraction window. In this figure, all spectra have been box-car smoothed by 41 pixels ($\sim$ 0.6 Å) for clarity. The emission feature is the O I complex near 989 Å.
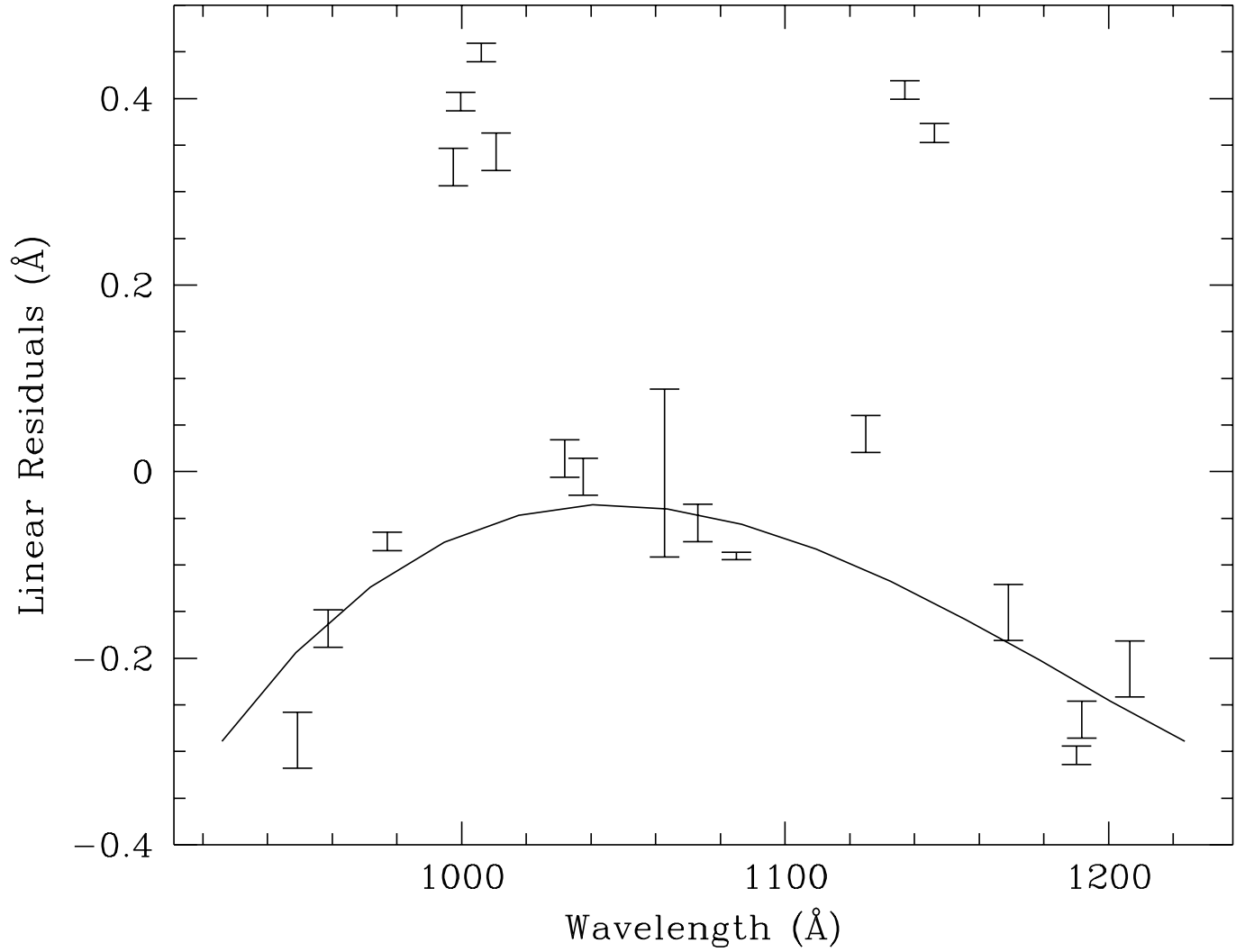
Fig. 4.— The BEFS wavelength calibration. The points mark the measured positions of emission features in the spectrum of RR Tel, plotted as residuals from a linear fit. The solid curve represents the deviation from a linear wavelength solution (wavelength minus linear fit) derived from an optical ray trace of the telescope and spectrometer. The solid curve has been shifted in both dimensions to reproduce the observed RR Tel wavelengths, excluding the sharp deviations around 1000 and 1140 Å. Additional wavelength points, derived from the spectra of white dwarfs and α CMi, are not shown.
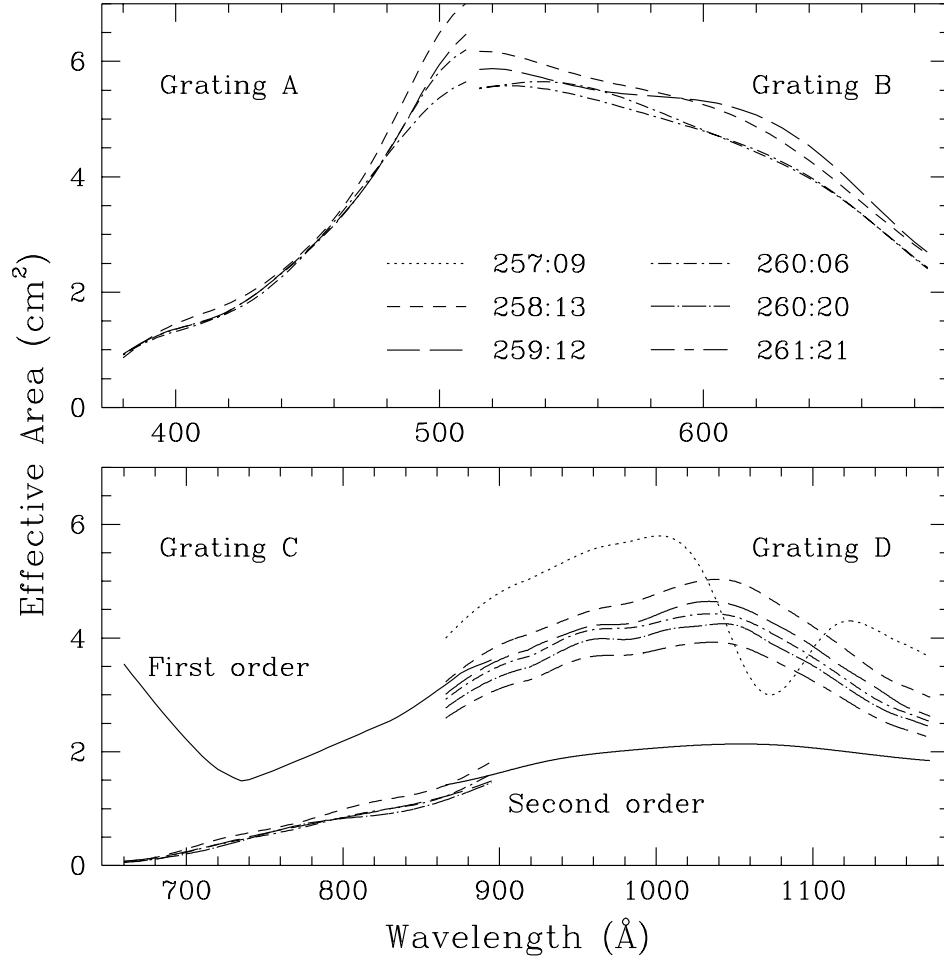
FIG. 5.— Effective-area curves for the BEFS on the *ORFEUS-SPAS I* mission, derived from observations of white dwarf stars, primarily G 191–B2B. Differences among the Grating A and D curves are thought to be real and reflect a decrease in sensitivity with time. Differences among the Grating B curves are not significant given the S/N ratios of the individual spectra; an average of the Grating B curves is applied to all spectra. The Grating C spectrum of G 191–B2B shows no first-order astrophysical flux; the curve presented is theoretical. The Grating D effective area shows a slow decrease in sensitivity with time; we interpolate among these curves to calibrate our data. Theoretical second-order curves are scaled to match the flux seen in spectrum C and in spectrum D below 912 Å.
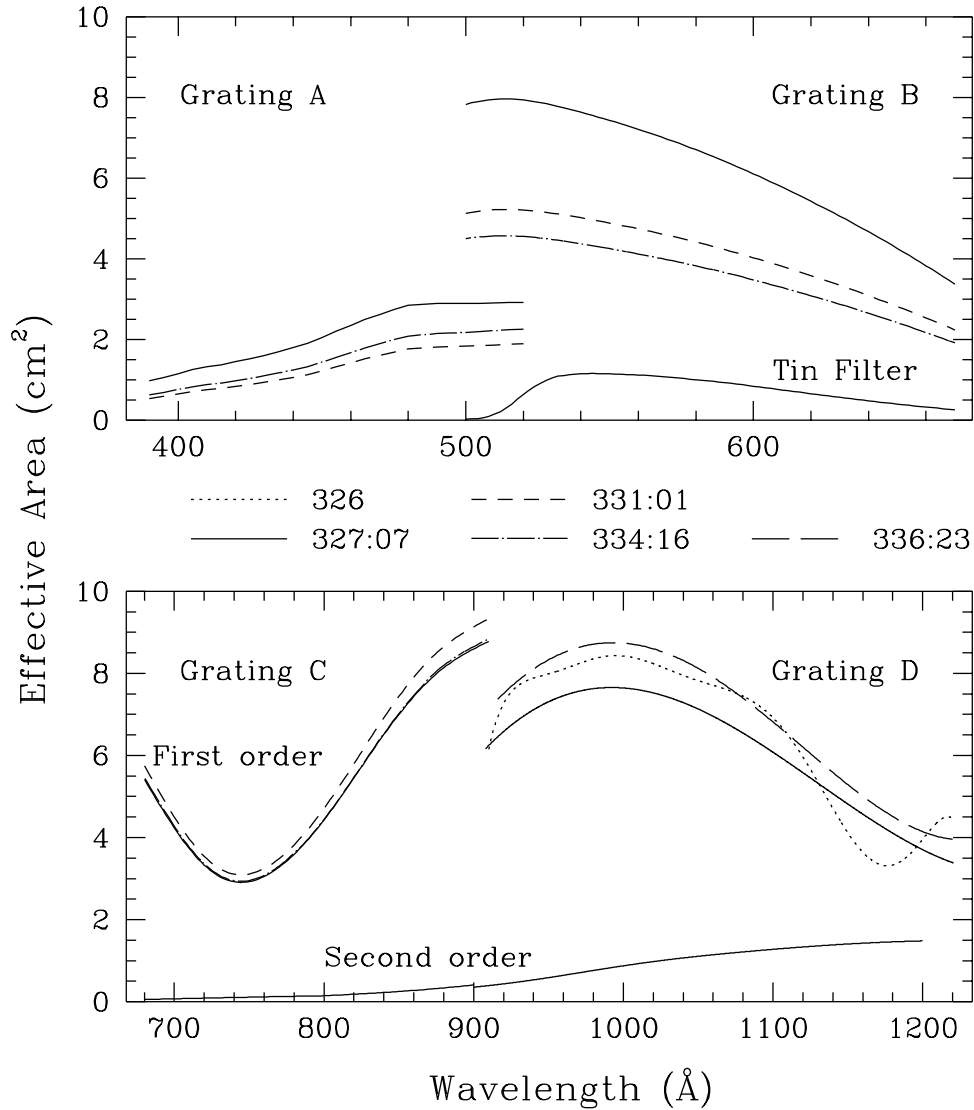
Fig. 6.— Effective-area curves for the BEFS on the *ORFEUS-SPAS II* mission, for which the principal flux-calibration target is HZ 43. The dramatic variation in the effective areas of Gratings A and B reflects the photometric problems that affect our observations at these wavelengths. Rather than attempting to correct for them, we adopt the first (highest) effective-area curve for all Grating A and B spectra. For Gratings C and D, we employ the curve obtained nearest in time to each observation. (We do not interpolate among the curves.) The second-order curves are derived theoretically and scaled to the observed second-order flux.
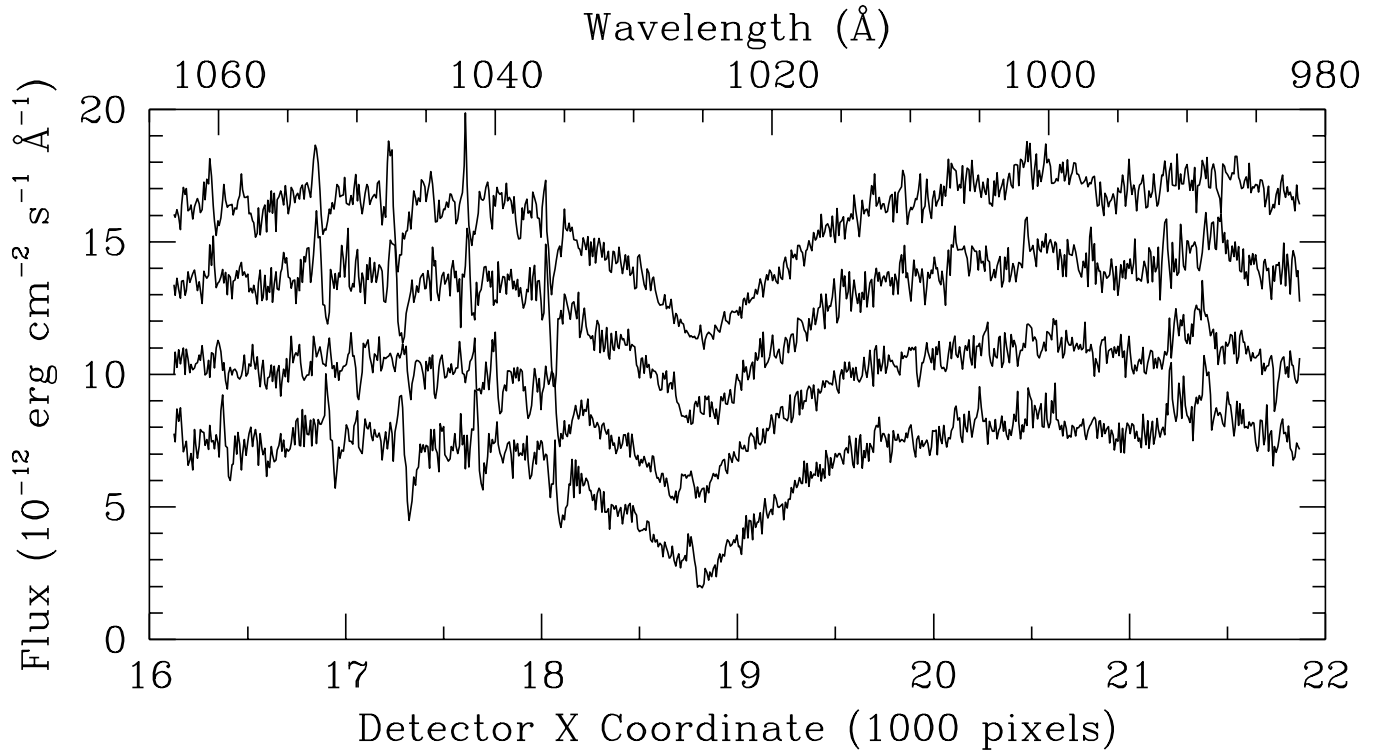
Fig. 7.— Flat-field effects in *ORFEUS-SPAS II* spectra of HZ 43. Note the four P Cygni-like features between 1035 and 1055 Å and the broad trough between 991 and 999 Å. These features are discussed in the text. From bottom to top, the spectra were obtained on GMT days 327, 331, 334, and 336. The flux of the bottom spectrum is correct; the others are offset in flux space for clarity. The data are binned by 8 pixels and are plotted in pixel space; the wavelength scale is approximate.
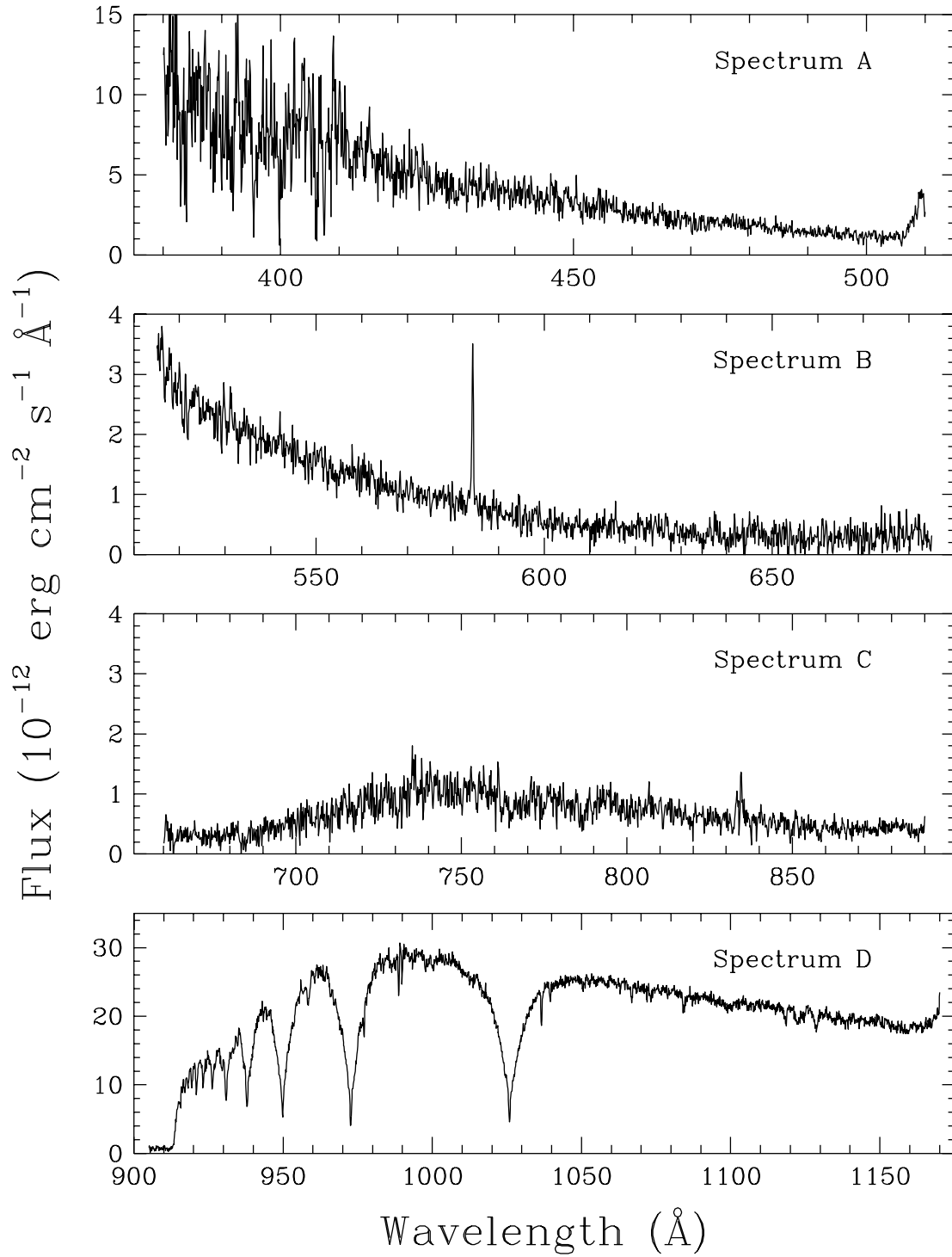
FIG. 8.— Complete spectrum of G 191–B2B obtained by the BEFS on the *ORFEUS-SPAS I* mission. Spectra A, B, and C are binned by 16 pixels, spectrum D by 8. Note the bright corner, which contaminates spectrum A at wavelengths shorter than about 420 Å, and the geocoronal He I λ584 and O II λλ832.7–834.5 features in spectra B and C, respectively. Most of the flux in spectrum C is second-order light from EUV wavelengths.
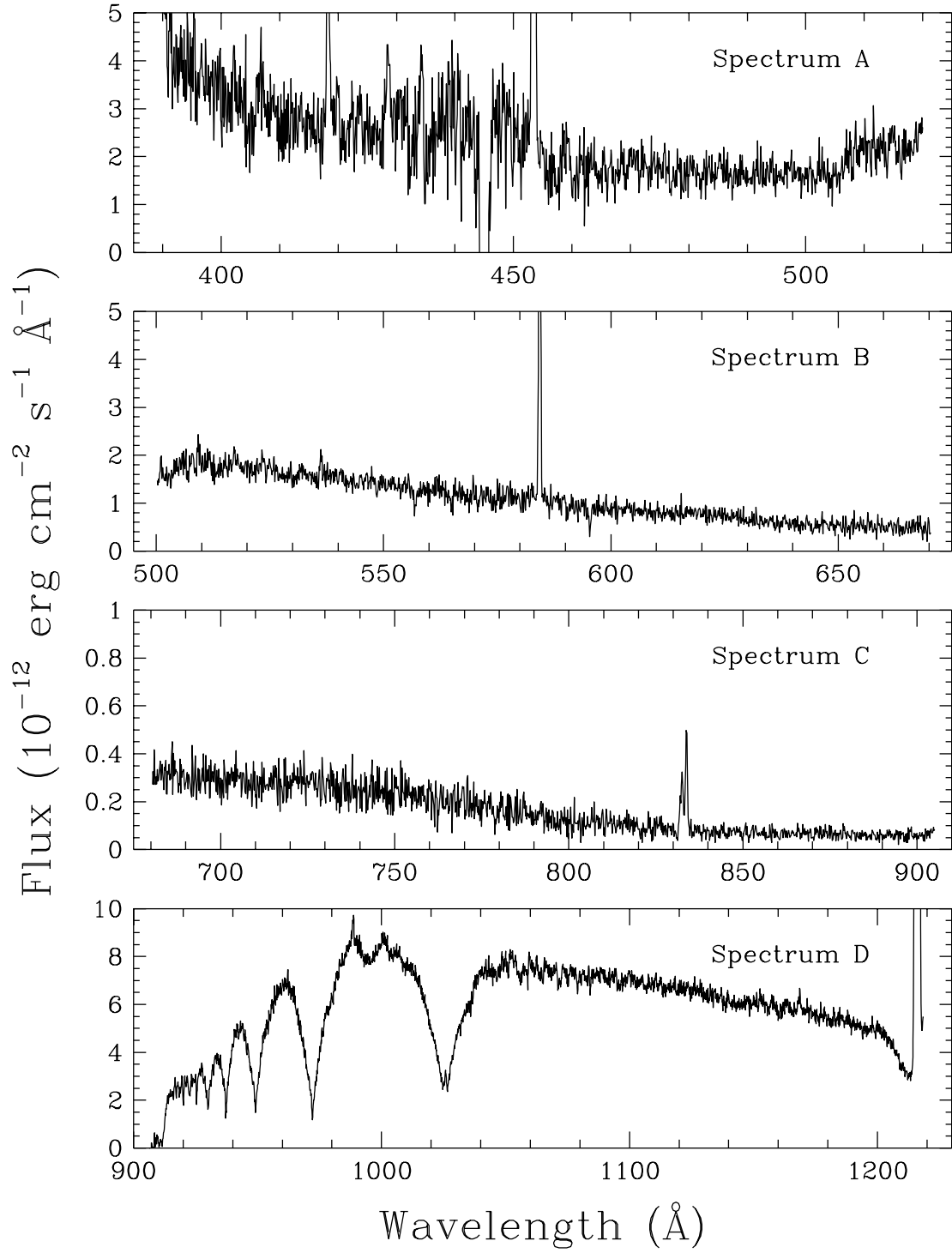
FIG. 9.— Complete spectrum of HZ 43 obtained by the BEFS on the *ORFEUS-SPAS II* mission. Spectra A, B, and C are binned by 16 pixels, spectrum D by 8. Because the spectra from Gratings A and B overlap in this data set, spectrum A is contaminated between about 400 and 460 Å (see discussion in text). The neutral-hydrogen column density toward HZ 43 is lower than that toward G 191–B2B, allowing first-order flux to reach us at the short-wavelength end of spectrum C.